Icarus 312 (2018) 231–246

Contents lists available at ScienceDirect

Icarus

journal homepage: www.elsevier.com/locate/icarus

The length of lunar crater rays explained using secondary crater scaling

Jacob R. Elliott*, Ya-Huei Huang, David A. Minton, Andrew M. Freed

Department of Earth, Atmospheric, and Planetary Sciences, Purdue University, West Lafayette, IN 47907, USA

ARTICLE INFO

Article history:
Received 26 September 2017
Revised 4 April 2018
Accepted 16 April 2018
Available online 18 April 2018

Keywords:
Cratering
Impact processes
Moon, Surface

ABSTRACT

The relationship between the length of crater rays and primary crater radius is still poorly understood. In this study we mapped the ray systems of 27 lunar craters, ranging from 10 m to 84 km in diameter. For each ray system, we measured the number, length, and optical maturity index (OMAT) of the rays. Our mapping effort shows that ray length scales to primary crater radius (R) with a power-law of $R^{1.22}$, except for the smallest and freshest rays (<10 m diameter craters, less than ~40 years old), which were ~10 radii longer than expected. We also undertook an analytical modeling exercise in an attempt to better understand the physical processes that control ray length. The model suggests that the empirical relationship ($R^{1.22}$) can be explained as resulting from the combination of 1) the relationship between ejecta fragment size and ejected distance, and 2) the scaling of secondary crater diameters, which create rays by excavating bright material from below the dark space-weathered layer, as a function of ejected velocity. When the ejecta fragments are large enough, they are able to excavate bright material from beneath the mature space-weathered layer, while smaller ejecta fragments simply mix the dark mature lunar soil. We then use this secondary crater scaling relationship to predict the ray length for different depths of well-weathered lunar soil. The anomalously long rays for the smallest, freshest craters may be due to the fact that their bright ejecta fragments are not traveling fast enough to excavate below the space-weathered surface layer, and simply become deposited on the surface. We suggest observations that will help refine many of the poorly constrained assumptions of our model.

1. Introduction

Rays are a ubiquitous feature seen predominantly around fresh craters, and are presumed to have formed around nearly all craters (Fig. 1). Visible crater rays diminish with time due to space-weathering and other erosional processes, so the initial extents of rays are poorly constrained. The process by which rays are generated from ejecta outflow is also poorly understood (Hawke et al., 2004). Studying the bright rays of Tycho using images with a resolution of only 300 m/px, Shoemaker (1965) noted that the density of secondary craters increased closer to the midline of each ray, suggesting that rays are due to clusters of bright secondary craters. Baldwin (1963) used a photometric study of lunar craters by Kuiper et al. (1960) to explore ray properties and compile a dataset of 50 lunar craters and their ray diameters. It is not specified what Baldwin meant by ray "diameter," however, attempts to reproduce his measurements suggest that he drew a line starting from the end of longest ray, going across the crater, and finishing at the end of a ray along this direction. Changing this diameter to radius is approximately equivalent to the median ray length. Moore et al. (1974) fit a power law function to Baldwin's data, however they mistook Baldwin's "Ray Diameter" data for the length of a single ray, leading to their fit being larger than Baldwin's data by a factor of 2. Refitting Baldwin's original data, we find that the median ray length (R_r) in kilometers could be empirically described by a power law function of the primary crater radius (R_p), also in kilometers:

$$R_r = 5.25R_p^{1.25}. \quad (1)$$

Within the last 10 years, the Lunar Reconnaissance Orbiter Camera (LROC), with a highest resolution of <0.5 m/px depending on the orbit, has been used to image the surface of the Moon in great detail. Small craters (<10 m in radius) can now be observed shortly after initial formation, allowing us to understand and study the freshest lunar crater rays before they decay (Robinson et al., 2015; Speyerer et al., 2016). Additionally, we can more closely examine older crater rays, enabling us to determine whether they ex-

* Corresponding author.
E-mail address: elliot26@purdue.edu (J.R. Elliott).

https://doi.org/10.1016/j.icarus.2018.04.015

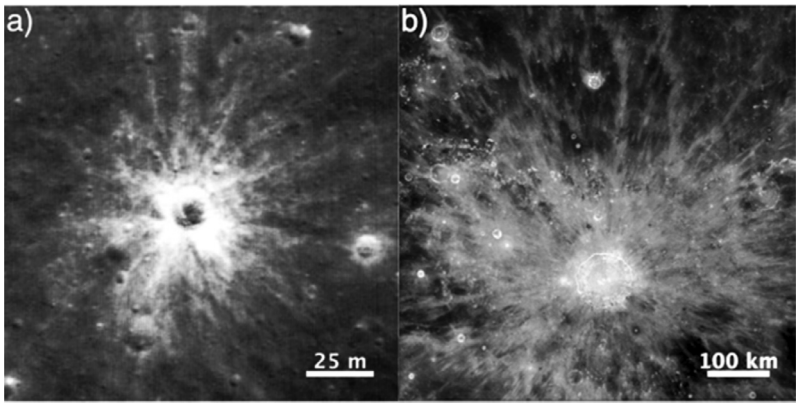

Fig. 1. Examples of lunar craters and their ray systems. (a) A 12 m-diameter fresh crater with a radial spoke pattern (LROC stamp: M170884438L). (b) Enhanced color contrast image of the 93 km-diameter Copernicus crater with an overlapping web pattern.

tend beyond Baldwin's estimates and determine whether his empirical relationship still holds.

Baldwin's empirical relationship motivates us to wonder what physical processes determine the exponent (1.25) of this equation. In order to explain why the visible albedo ray length increases nonlinearly with absolute crater size, we propose a hypothesis that the non-linear scaling between ejecta fragment size, ejected/landing velocity of fragments, and primary crater size produces similar-sized secondary craters at disproportionally farther distances with increasing primary crater size. Our hypothesis is tested by first mapping lunar craters and their ray systems using LROC images, cataloging ray length, number of rays per crater, and measuring relative crater age (OMAT index). We then re-examine Baldwin's fit to these new data to determine whether a new empirical relationship is warranted. Finally, we derive an analytical expression for ray lengths using observations of Censorinus crater. Our analytical model describes a possible relationship between the depth of the space-weathered upper layers of lunar soil and the mechanisms by which ejecta deposits create visible rays.

2. Ray origin

Studies of images from Ranger VII (Shoemaker, 1965), Earth-based telescopes (Pieters et al., 1985), the Apollo Panoramic Camera (Dundas and McEwen, 2007), and LROC (Hiesinger et al., 2012) confirm that distal rays are a mixture of primary crater ejecta and the ejecta of secondary craters (Fig. 2). Ejecta from the primary crater impact the surface and creates secondary craters, and thus excavate immature (higher-albedo) local materials that were buried and thus less space-weathered than the surrounding surface material.

As surface material weathers due to exposure to solar wind implantation (Zeller and Ronca, 1967) and sputtering (Hapke, 1973), micrometeorite bombardment (Cassidy and Hapke, 1975), and solar cosmic rays (Zeller and Ronca, 1967), it becomes darker in color (Pieters et al., 2000; Pieters and Noble, 2016). As the surface is gardened by both small-scale and micrometeorite impacts (Robinson et al., 2015; Werner and Medvedev, 2010), newly exposed grains experience weathering. Based on soil gardening rates and space-weathering timescales, this eventually leads to a relatively thin layer of weathered regolith that we will refer to as the space-weathered "skin." Estimations of the depth of this skin layer vary, with initial estimates on the scale of ~5 mm (Borg et al., 1976). However, analysis of returned lunar samples reveal a skin that is several cm to one or two meters thick (Haiken et al., 1991). Robinson et al. (2015) examined images of a recent crater's ejecta blanket, finding that the bright continuous ejecta blanket likely formed due to unweathered material excavated by the primary crater. The excavation depth of this material is expected to be one or two meters below the surface. Secondary craters must excavate material from below this skin depth in order to bring bright material to the surface. As secondaries become smaller, they will be of insufficient size to excavate less-weathered material, leading to secondary crater fields that are indistinguishable from the surrounding surface. This region is described as the "Distal Low Reflectance Zone in Robinson et al. (2015) and Speyerer et al. (2016). In our model, this transition between excavation zones will correspond to the maximum extent of the visible ray.

There are, however, some bright patches within a ray that do not appear to be associated with visible secondary craters. These have been interpreted as isolated patches of primary crater ejecta (Hawke et al., 2004). This primary crater ejecta may be excavated immature soils that are deposited on the darker mature surface. There may also be compositional differences between ejecta and the underlying surface, such as highland anorthosite ejecta deposited on mare basalt (Hawke et al., 2008, 2007, 2004). There is an inherent difference in brightness between materials of different composition. These primary ejecta patches are also seen surrounding smaller craters, where the ejection velocity may not be great enough to produce visible secondary craters.

It is possible for the above two mechanisms (soil maturity and compositional differences) to influence the same ray system. In this scenario, immature and compositionally brighter material is deposited atop a more mature, darker surface. As the deposited material matures, it begins to darken. However, because space-weathering cannot affect the compositional brightness, the ray system becomes purely compositional in nature (Hawke et al., 2004).

3. Ray mapping

To understand ray properties (e.g., number per crater, average length) as a function of primary crater size, we mapped systems of rays using the JMARS (Java Mission-planning and Analysis for Remote Sensing) software tool, a geospatial information system containing data sets for various planetary bodies (Dickenshield et al., 2015). We mapped rays of 27 craters with radii ranging from 5 m (youngest observed) to ~43 km (Tycho crater) (Table 2). The 27 craters were selected to provide a variety of crater sizes. Specific craters were selected because of their easily distinguished ray systems and coherent ray structure. A preference was given to craters with radial rays (Jackson crater) as opposed to more web-like patterns (Copernicus crater). Craters with compositional rays, such as Lichtenberg (Hawke et al., 2004), were avoided as our analytical model will focus solely on rays formed by secondary cratering

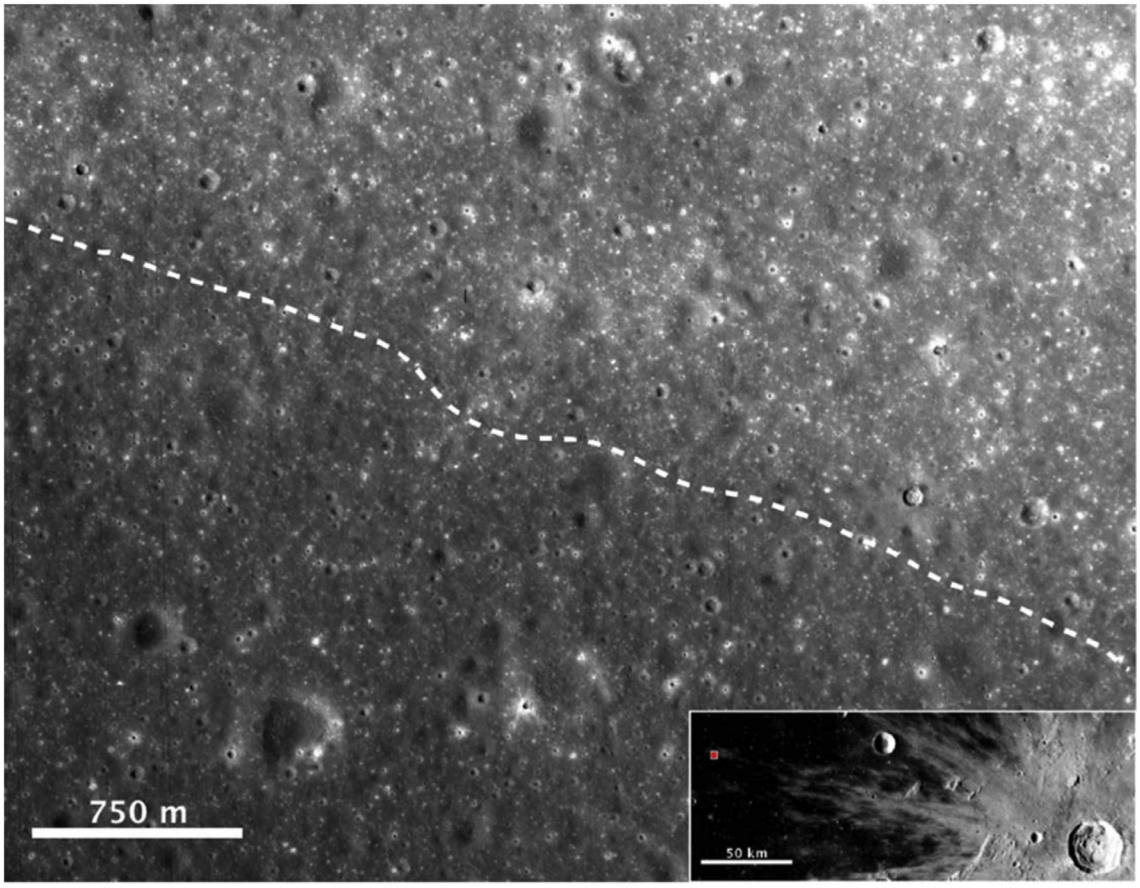

Fig. 2. A high-resolution (~50 cm/px) image of the edge of one of Kepler's rays (red point in inset). The area above the dashed line is located within the ray and contains an abundance of bright secondaries. When viewed at a lower resolution, these craters blend together, brightening the surrounding area, giving the appearance of a continuous bright streak. (For interpretation of the references to color in this figure legend, the reader is referred to the web version of this article.)

For smaller craters (< 600 m in radius) we used LROC Narrow Angle Camera images with a resolution of ~0.5 m/px, allowing us to map craters as small as 5 m in radius (possibly smaller). When viewing these images, JMARS allows for exposure/contrast control, which was used to isolate ray features from the background surface. Unfortunately, this data set is not normalized for sun incidence angle. This leads to some ray systems appearing indistinguishable from the lunar background and thus unmappable. The lack of normalization may have influenced the observed ray lengths as rays are generally less visible and thus shorter under high sun-incidence angles (Neish et al., 2013). To confirm this effect, we examined crater M110757216LE under three different sun-incidence angles (Fig. 3). We found that rays are more clearly defined with low-incidence angles (~20°). The visible ray length does not appear to change at ~32°, however some detail is lost. At ~60°, the ray system was indistinguishable from the lunar background. High-incidence angles were avoided, but some craters have only been imaged at high angles. Incidence angles and pixel scales are found in Table 1.

For larger craters (>600 m in radius), LROC Wide-Angle Camera Normalized Reflectance 643 nm images were used, which have a resolution of 100 m/px (Robinson et al., 2010). For these images, JMARS does not allow for easy manipulation, such as contrast stretching and brightness adjustment. Instead, these images were contrast stretched in Adobe Photoshop and uploaded to JMARS using its Custom Map feature. These products are normalized for reflectance, meaning post-processing has been done in order to give the appearance of a directly overhead sun (Bowman-Cisneros and Isbell, 2008; Murphy et al., 2010).

Table 1
Pixel scales and incidence angles for every NAC image used in our study.

Image/Crater Name	Pixel Scale [m/px]	Incidence angle
M108971316LE	0.51	18.12
M1101530748RE	1.06	29.18
M1136364148RE	0.90	35.58
M104913277RE	1.12	47.94
M110757216LE	0.61	23.6
M1172454326LE	2.14	79.54
M106490422RE	1.20	30.59
M104913277RE	1.12	47.94
M1100631156LE	0.95	22.13
M1146499672RE	1.09	23.77
M1123988696LE	2.14	72.93
M1118944656RE	1.04	32.6
M104913277RE	1.12	47.94
M1139022745RE	1.33	69.41
M1095544821RE	1.22	84.64
M1146499672RE	1.09	23.77
M1159450887RE	1.07	52.06

Potential rayed craters were identified by eye from the LROC Normalized Reflectance images. Larger rayed craters were easy to identify as they spanned many pixels, while smaller rayed craters were initially identified as bright splotches in the Normalized Reflectance images and were then further examined using Narrow Angle Camera images. Once a ray system was identified, a circle was fit to the primary crater's rim, which gave us a measure of the crater's radius and center position in terms of latitude and longitude. Each ray was then outlined using the custom shape tool of

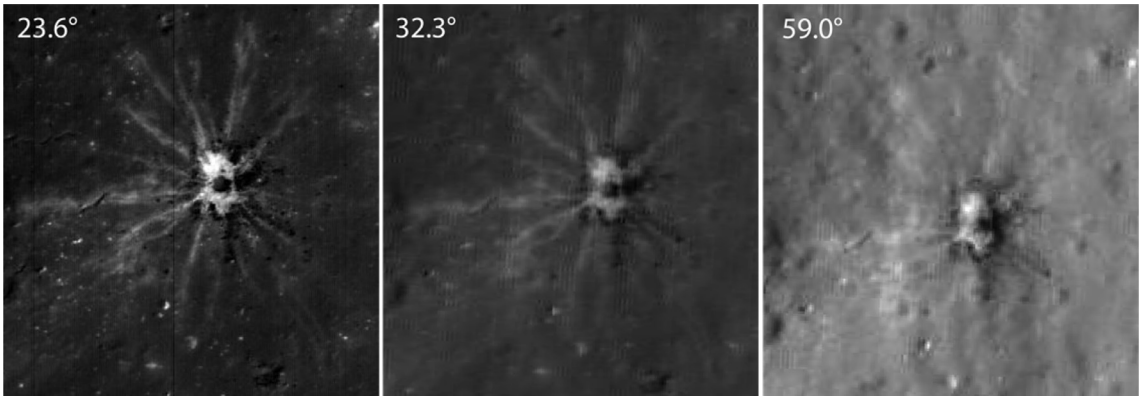

Fig. 3. A comparison of ray visibilities with changing sun-incidence angles. Crater M110757216LE was examined under 23.6°, 32.3°, and 59.0° incidence angles. It is clear that ray visibility degrades substantially at higher incidence angles.

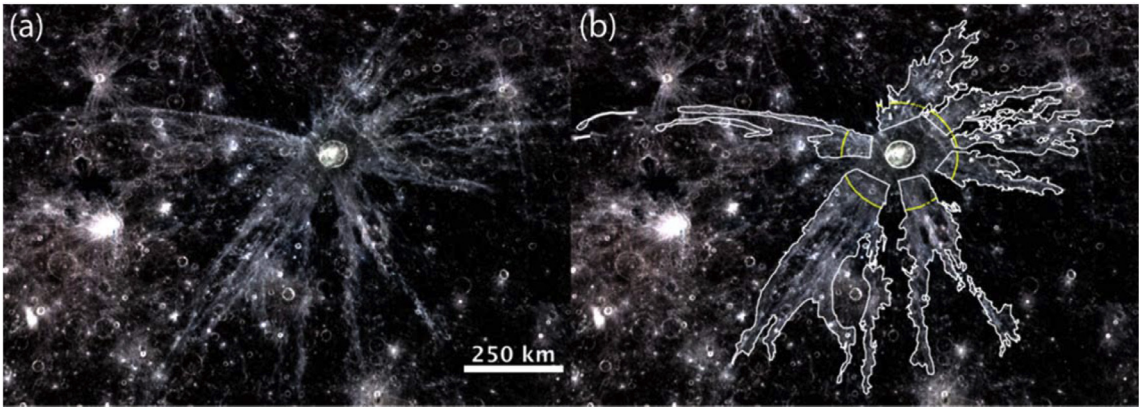

Fig. 4. (a) Jackson crater, unmapped. (b) Jackson crater, mapped, with OMAT measurements displayed in yellow. Note the detached ray segment on the left edge. These segments were included in measurements. The base image is LROC Normalized Reflectance 643 nm. It has been stretched to better differentiate rays from lunar background. (For interpretation of the references to color in this figure legend, the reader is referred to the web version of this article.)

JMARS. This outline started slightly within the continuous ejecta blanket and continued to the end of the visible ray (Fig. 4b). Note that the exact start of the outline is not of importance, as this study only seeks to determine the ending location of the ray relative to the crater center. It is likely that the ray begins at the crater rim itself (Krishna and Kumar, 2016). Detached segments were included in the measurements if they could be traced back to the primary crater or appeared to connect to a more continuous ray (see left side of Fig. 4b). Isolated clusters, such as those found surrounding Tycho (Dundas and McEwen, 2007), were ignored as we focused on the ray structure rather than individual secondary clusters. Gaps within the ray system were ignored if the ray reappeared downrange. If a ray began as a single, cohesive ray but eventually split into multiple rays, it was counted as multiple individual rays. For example, the rays at the 5 o' clock position in Fig. 4b were counted as two rays, even though they merge together near the crater rim. There is room for error in this process as there is no definitive boundary between ray and the lunar background. Once mapped, the Haversine formula was used to calculate distance from the center of the primary crater to the end of the ray.

In order to understand how space-weathering affects ray systems, the relative ages of the craters must be known. To accomplish this, we make use of the optical maturity index (OMAT) that takes into account Fe ratios and reflectance at 750 and 950 nm (Lucey et al., 2000). While there is a newer OMAT dataset from the Kaguya Multiband Imager (Lemelin et al., 2016), we choose to use the Clementine dataset as it is already integrated into JMARS and previous studies have provided reference OMAT values that we can compare our work to (Grier et al., 2001). It is expected that young, brighter craters will have higher OMAT values than older craters (Grier et al., 2001, 2000; Lucey et al., 2000). For example, Grier et al. (2001) measured Tycho's OMAT value to be 0.278, and Copernicus's to be 0.178. Tycho is estimated to be fairly young (109 Ma), while Copernicus is older (782 Ma) (Hiesinger et al., 2012). Newly examined craters can be placed into a relative chronological order based on their observed OMAT values. There does appear to be a size bias associated with OMAT measurements, with smaller craters having darker ejecta and less immature blankets than larger, equivalently aged craters (Grier et al., 2001). This leads to a presumed undercount of young, 1–10 km craters. OMAT values were obtained from the Clementine UVVIS/Optical Maturity data set at a resolution of 200 m/px. For each crater, all points within rays were sampled at a distance of 4 radii away from the crater center (Fig. 4b). The measurement distance of 4 radii was chosen to match the measurement distance of Grier et al. (2001), whose data are used as calibration for our relative ages. The dataset's coarse resolution means that small craters cannot be assigned an age. These craters are marked "N/A" in Table 2. The two smallest craters have formed since Apollo images and are therefore assigned an OMAT of ">0.25".

Based on the 27 craters studied here (Table 2), craters have an average of 10.7 rays, ranging from 2.2 to 52.5 radii in length. The average ray width, which is defined as the polar angle of a ray at 2 radii from the center of the crater (as continuous ejecta break down into a ray structure), is 22° with a standard deviation of 8.3°.

Table 2
Summary data of the crater ray mapping process. Small unnamed craters were named using the LROC image stamp in which they were found.

Crater Name	Radius [km]	Lat.	Long.	Number of Rays	Median length [km]	Maximum ray length [km]	Minimum ray length [km]	OMAT
M108971316LE	0.005	16.925	40.504	8	0.05	0.06	0.02	>0.25
M1101530748RE	0.006	25.113	310.447	14	0.08	0.12	0.05	>0.25
M1136364148RE	0.006	−12.177	29.723	8	0.02	0.03	0.02	N/A
M104913277RE	0.007	−1.106	299.721	11	0.07	0.11	0.05	N/A
M110757216LE	0.015	12.928	127.668	11	0.04	0.10	0.03	N/A
M1172454326LE	0.015	−1.763	91.808	13	0.08	0.12	0.05	N/A
M106490422RE	0.019	−6.781	58.821	10	0.09	0.11	0.06	N/A
M104913277RE	0.021	−1.011	299.678	11	0.10	0.13	0.06	N/A
M1100631156LE	0.029	1.624	87.647	10	0.07	0.14	0.05	N/A
M1146499672RE	0.049	−1.205	99.951	10	0.14	0.21	0.10	N/A
M1123988696LE	0.064	0.182	299.910	8	0.22	0.34	0.15	N/A
M1118944656RE	0.098	31.055	351.216	9	0.29	0.43	0.16	0.19
M104913277RE	0.10	−1.236	299.725	14	0.46	0.78	0.28	0.18
M1139022745RE	0.13	26.460	341.778	10	0.44	0.65	0.39	0.21
M1095544821RE	0.21	−56.184	146.758	7	1.06	1.24	0.95	0.25
M1146499672RE	0.23	−1.248	99.923	9	1.45	1.96	0.97	0.19
M1159450887RE	0.25	−0.730	99.929	8	1.44	1.62	0.83	N/A
NE of Condon	0.68	2.209	60.824	13	4.61	8.29	3.32	0.18
S of Apollonius	0.76	2.208	60.823	13	4.44	8.00	3.30	0.17
NW of Bohr	1.4	14.137	271.988	13	14.02	26.71	10.36	0.21
SW of Kearons	4.2	−12.477	246.070	9	47.92	74.35	33.53	0.21
SE of Ritz	4.8	−16.953	93.924	6	110.55	154.64	83.23	0.20
Kepler	15	8.083	321.990	16	253.17	448.04	182.68	0.22
Anaxagoras	26	73.481	349.835	20	334.92	662.99	214.10	0.27
Jackson	36	22.005	196.668	12	596.32	786.04	383.80	0.22
Tycho	42	−43.305	348.781	8	801.29	2202.98	606.84	0.25

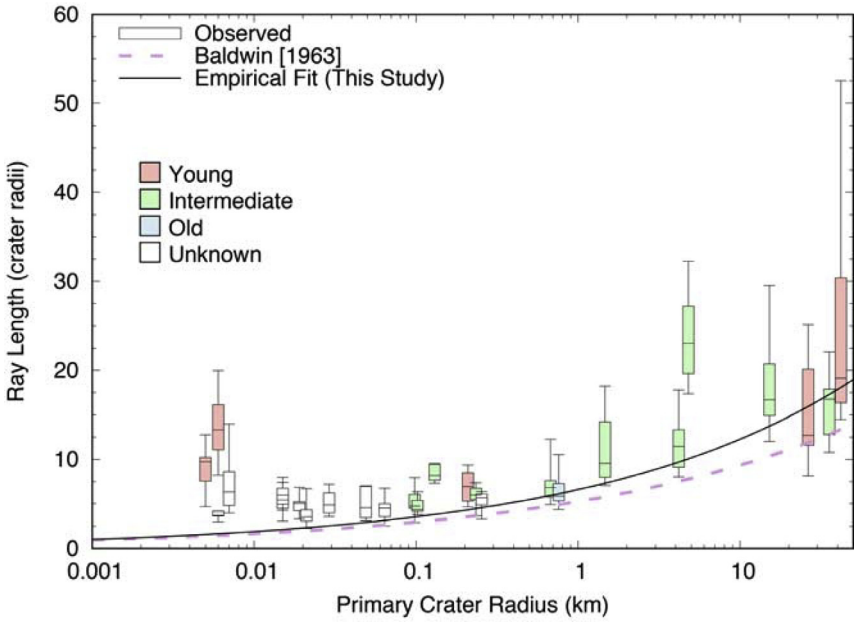

Fig. 5. The distribution of lunar crater ray length against primary crater radius. The box and whisker plots contain the distribution of ray lengths for each mapped crater. The color fill represents the crater's age based on OMAT value (young: ≥ 0.22, intermediate < 0.22 and ≥ 0.18, old: < 0.18). Whiskers mark the maximum and minimum ray length. 50% of the crater's rays are within the box. The purple dashed line denotes Baldwin's (1963) empirical fit. The solid black line denotes our new empirical fit. (For interpretation of the references to color in this figure legend, the reader is referred to the web version of this article.)

Ray lengths vary significantly with size, demonstrating increasing length with increasing primary crater size (Fig. 5).

As each individual crater is unique, some variation in ray lengths is caused by impact conditions, such as different local target surface properties and topography which may have affected its ejecta deposition. The largest source of variation in the lengths of rays for a single crater is caused by the fact that most impacts occur at an angle relative to local surface. Laboratory and numerical experiments have shown that oblique impact at less than 45° results in an avoidance zone, or lack of ejecta, in the uprange direction, and a greater concentration of ejecta downrange, with a second avoidance zone appearing downrange at angles less than ~10° (Elbeshausen et al., 2013; Gault and Wedekind, 1978; Richardson, 2011; Schultz and Anderson, 1996). Herrick and Forsberg-Taylor (2003) surveyed craters on the Moon and Venus, finding that there are several key angles at which the ejecta blanket is modified: at <45° the blanket is asymmetric; at <25° an uprange avoidance zone develops; and at <10° a downrange avoidance zone develops. Ejection velocities are also modified, with downrange material being ejected with 20–40% higher velocities than uprange ejecta (Anderson and Schultz, 2003). The combination of greater ejection velocities and ejecta concentrations results

in longer rays in the downrange direction. To account for this effect, we use the median ray length, as opposed to the maximum, in our calculations. Because ejecta is modified by impact angle in an axially symmetric fashion, the median length of the ray system is approximately what the length of all of the rays would be had the impact been vertical rather than oblique (Richardson, 2011).

We fit a power-law curve to these ray systems using the median ray lengths for each crater. A power-law fit was chosen because we are trying to make a direct comparison to Baldwin's (1963) fit. Other fits were tested and performed roughly equally to a power-law. Craters below ~100 m in radius were excluded from this fit as they are clearly anomalous to the trend of larger craters (we discuss possible reasons below). We find a relationship between ray length and primary crater radius is empirically described by:

$$R_r = 6.59(\pm 2.9)R_p^{1.27\ (\pm 0.12)}, \tag{2}$$

with 2σ uncertainties shown in parentheses. The 2σ uncertainties were calculated using a non-linear least-squares method, which assumes a normal distribution of errors. The fit has an R^2 value of ~0.99. The exponent (1.27) is similar to Baldwin's (1.25), and within the uncertainty. The nominal scaling factor (6.59) is larger than that suggested by Baldwin (5.25), but is also within the uncertainty. These two equations are plotted over the mapped ray data in Fig. 5. Our modestly larger exponent leads to a slightly longer predicted ray length as a function of primary crater radius for the largest craters.

Other differences may be due to Baldwin's measured ray length for the larger craters, such as Kepler and Tycho, being longer (~250 km and ~1000 km, respectively) than our measurements. This disparity may be due to the differing image resolutions, where Baldwin's lower resolution may have made it easier to conflate rays of different craters, leading to erroneously longer rays. On the other hand, our higher resolution images may have led to shorter inferred rays by more easily identifying where the lunar background material becomes more pronounced within a ray. A larger number of small rays will also bring down the median. Tycho, for example, has few long rays pointing to the north and many shorter rays pointing to the south. It is suspected that this discrepancy in ray orientation is due to an oblique impact (Krüger et al., 2016). The large number of smaller rays decrease the median, skewing our results from those of Baldwin. Despite these differences in measured lengths, the equations are still quite similar, with a −4% (0.4 km) difference in ray lengths for a 1 km-radius crater, and a +8% (107 km) difference in ray lengths for a 50 km-radius crater, with our fit predicting longer lengths for the 1 km crater and shorter lengths for the 50 km crater.

4. Secondary crater scaling model derivation

Because non-compositional, distal rays are composed of numerous secondary craters and their ejecta blankets (Fig. 2), the visibility of a crater's ray should be related to the size and spatial density of its secondary craters. Consider two craters, one large and one small, that each deposits an ejecta fragment whose size and downrange distance are proportional to their primary craters' radius. Because the larger crater's ejecta fragment travels a longer distance, it will impact the lunar surface at a higher velocity. The secondary crater produced by the larger primary's fragment will thus be proportionally larger than the secondary crater produced by the smaller primary's fragment. Our hypothesis is that the maximum distance at which secondary craters will excavate bright, unweathered material determines the visible ray length, and should scale with primary crater size in a way defined by our empirical relationship given in Eq. (2).

In this section we derive an analytical model to explain our observational data. This analytical model depends on primary crater size and the depth of the space-weathered skin. In Section 4.2 we explore the model variables and discuss their constraints. In Section 4.3 we evaluate what variables result in a match with the observational data. Finally, in Section 4.4 we discuss limitations of this analytical model and suggest observations needed to constrain future models.

4.1. Analytical model

To explain our observational data, we seek to derive a physical explanation for ray length, R_r, as a function of primary crater size, R_p, depth of the mature lunar soil, h, and the probability, P, that a given area is excavated to that depth h:

$$R_r = f(R_p,\ h,\ P). \tag{3}$$

To accomplish this, we will first derive an equation for secondary crater size, R_s, as a function of distance, r, and fragment size, D_f. We then use observational data from Krishna and Kumar (2016) to estimate the ejecta fragment size-frequency distribution (SFD) $N(D_f)$ at distance r for a given primary crater size R_p. This will give a size-frequency distribution for secondary craters, $N(R_s)$. We will use the expression for $N(R_s)$ to determine the probability that the surface at downrange distance r has been excavated to depth h. We can then solve for the downrange distance R_r at which the excavation depth h is equal to the space-weathered skin depth, which is the length of the ray.

We begin with a crater scaling law developed in Schmidt and Housen (1987):

$$R_s = k\left(\frac{\delta}{\rho}\right)^{\frac{1}{3}} {D_f}^{1-\beta} g^{-\beta} {v_i}^{2\beta}, \tag{4}$$

where $k = 0.625$ is an empirical crater scaling constant for dry sand (see Tables 1 and 3 in Schmidt and Housen, 1987), β is a constant 0.17 for dry sand (see Table 3 in Schmidt and Housen, 1987), δ is projectile density, ρ is target density, D_f is projectile diameter (assuming a spherical shape), g is gravitational acceleration, and v_i is impact velocity (assuming a vertical impact). However, we assume an impact angle of 45°. Therefore we multiply k in Eq. (4) by $\sin^{1/3}45°$ (Gault et al., 1974), giving $k = 0.5568$. Impact velocity v_i can be expressed in terms of distance r using a simple ballistic trajectory where we assume a flat surface and that impact velocity is equal to ejection velocity:

$$\sqrt{\frac{gr}{\sin(2\theta)}}, \tag{5}$$

where θ is the impact angle, assumed to be 45°, which eliminates the denominator. We assume a flat surface as the effect of the curved surface is negligible when distance is much less than the radius of the planetary body (Burko and Price, 2005; Shuvalov, 2012). We make this approximation as most rays, except those of Tycho-sized craters, are relatively short compared to the Moon's radius. It is assumed that ejecta originate at the crater center, as ejecta departing from the center generally have the highest velocities. We assume the radial distance in the origin location within the excavation zone between fragments at escape velocity and subescape velocity to be negligible. Inserting (5) into (4) and simplifying:

$$R_s = k\left(\frac{\delta}{\rho}\right)^{\frac{1}{3}} {D_f}^{1-\beta} r^{\beta}, \tag{6}$$

where r is distance from the center of the crater. Because the impact velocity of the distal ejecta fragments that make up the ray are directly related to their downrange distance, which can be expressed as a power law, we expect that the size of the secondary craters that make up the rays will not scale linearly with the size

of the primary crater, even if we assume that the size of the ejecta fragments does.

Eq. (6) describes a crater scaling law for a single cratering event. It would not be appropriate to use this equation alone to describe a ray forming event. This is because rays are usually associated with a secondary field or a cluster of boulders. We must therefore consider the size-frequency distribution (SFD) of distal ejecta fragments. We assume that the SFD of the fragments that generate the ray follows a power law function with power index of b. Some combination of number and size of distal ejecta fragments determines the size of the secondary crater field that makes up the ray. To model this, we use Poisson statistics to describe the probability (P) that any point on the surface inside a ray is occupied by craters given some assumed distal ejecta fragment SFD. It should be noted that secondary cratering is not strictly governed by classical Poisson statistics due to clustering. However, we will restrict our analysis to the centerline of the ray. With an appropriate model for an ejecta fragment SFD that does not vary greatly along the centerline of the ray, Poisson statistics should be adequate for our purposes.

Considering a fragment size range between R_{min} and R_{max}, this probability is:

$$P = 1 - \exp\left[-\int_{R_{min}}^{R_{max}} \frac{dN(R_s)}{dR_s} \pi x^2 dR_s \right], \quad (7)$$

where $N(R_s)$ is the cumulative size-frequency distribution (CSFD) for craters, and $\frac{dN(R_s)}{dR_s}$ is the number of craters that fall within the range of R_s and $R_s + dR$ that form per unit area, and x is the distance from the center of the crater, so πx^2 is the fraction of the crater that is excavated to depth h.

In order for a ray to be visible, it must be composed of secondary craters that can excavate unweathered material. To describe a visible ray, we must include excavation depth in Eq. (7). To model this we assume that the secondary crater excavation zone has a parabolic shape. A radial distance, x, from the center of a crater with radius R_s describes an excavation depth. For example, at the center of a crater, the excavation depth (h) is the deepest, $R_s/4$ (h_{excav}). We assign h_{excav} as equal to $2\alpha R_s$, in which α is 1/8, the maximum excavation depth of a streamline (Gault et al., 1974).

$$h = \begin{cases} h_{excav}\left(1 - \frac{x^2}{R_s^2}\right), & x < R_s \\ 0, & x \geq R_s. \end{cases} \quad (8)$$

We can substitute the variable of x^2 in Eq. (8) into Eq. (7) and rewrite it as:

$$P(h) = 1 - \exp\left[-\int_{R_{min}}^{R_{max}} \left| \frac{dN(R_s)}{dR_s} \right| \pi R_s^2 \left(1 - \frac{h}{2\alpha R_s}\right) dR_s \right]. \quad (9)$$

Eq. (9) describes the probability P that a point on the surface within a ray is excavated to a depth h by secondary craters in the size range $R_{min} < R_s < R_{max}$. R_{min} is the smallest sized secondary crater that will excavate to depth h, which is the depth of the mature layer, and create a ray. Secondaries smaller than this will only rework the surface.

Our hypothesis is that the length of visible albedo rays is related primarily to the fact that the distal ejecta landing velocities do not scale linearly with primary crater size. This creates proportionally larger secondary craters at any given relative downrange distance r/R_p. We derived Eq. (9) to describe the relationship between the excavation depth of secondary craters in a ray and the distal ejecta fragment size-frequency distribution, but now we have to incorporate how the ejecta fragments change with downrange distance r. We can characterize the fragment SFD using a cumulative power law function of the form:

$$N_{>D_f}(r) = C(r) {D_f}^{b}, \quad (10)$$

where $C(r)$ is the total number of fragments at a given distance r, D_f is the fragment diameter, and b is a power-law index of the fragment SFD.

Although our hypothesis is that the exponent in our empirical fit, Eq. (2), is controlled primarily by the non-linear scaling of ejecta landing velocities with primary crater size, given by Eq. (5), we will assume for the sake of developing our model that our distal ejecta fragment SFD given by Eq. (10) *does* indeed scale linearly with primary crater size. If we cannot find a plausible ejecta fragment SFD that results in the observed relationship between visible ray length and primary crater size, then our hypothesis is unlikely to be correct.

We will use observations of the SFD of ejected boulders in one very well characterized impact crater as a constraint on our distal ejecta fragment SFD model given by Eq. (10). We use data from Krishna and Kumar (2016) who counted 242,000 boulders within ~4 radii surrounding Censorinus crater (~3.8 km-diameter), which includes the region where the ejecta transition from continuous to discontinuous. Note that there are likely differing processes involved in continuous ejecta blanket boulder production and distal ejecta production. Unfortunately, the boulder density of distal ejecta is poorly constrained. For the purpose of this study we assume that there is no difference between proximal and distal ejecta. Furthermore, a clustered impact may involve multiple fragments impacting close to each other and forming what appears to be a single crater (Schultz, 1992). We caution that our model does not directly address this effect and likely over-predicts the number of secondary craters.

Krishna and Kumar (2016) divided the boulder field of Censorinus crater into four concentric sectors and 128 subsectors in total. They obtained the boulder density and the power-index of the boulder CSFD from each subsector. We fit a power law function to the mean spatial density of boulders (Fig. 13a of their study) vs distance with a power index of a,

$$n_b = n_0 \left(\frac{r}{R_{ref}} \right)^a, \quad (11)$$

where R_{ref} is the radius of the reference crater and n_0 is the number of boulders >3 m in diameter per m^2 (see Section 4.2.1). We assume that the spatial density of boulders in distal rays beyond 4 radii is uncertain. Although there are variations in boulder density from a subsector at a given distance, the general trend between mean boulder density and distance is described by Eq. (11). The mean spatial density of boulders we derived from (11) is treated as the total spatial density of boulders within a ray at a distance and obtained,

$$C(r) = n_0 \left(\frac{r}{R_{ref}} \right)^a {d_{boulder}}^{-b}. \quad (12)$$

This was done by solving Eq. (10) for $C(r)$. $N_{>D_f}(r)$ is equal to n_b from Eq. (11) and D_f is set to be $d_{boulder} = 3$m, which is the minimum boulder size used in Krishna and Kumar (2016).

The spatial density of boulders is likely dependent on primary crater size. However, the boulder densities in Eqs. (10) and (11) are based on a single study of one crater. As we hope to extend this relationship to any size of crater, we need to transform Eq. (11) to reflect both the distances and the total boulder density, scaled by a given size of crater. Because the relationship between ray length and primary crater size is well characterized by a power law, this transformation should also scale by some power law. Thus we begin this process by multiplying Eq. (11) by a scaling factor $(\frac{R_p}{R_{ref}})^c$, where R_p is the radius of some primary crater and R_{ref} is the radius of a reference crater, and c is constrained from observations,

which will be discussed in Section 4.2.4. Eq. (11) then becomes:

$$n_b = n_0\left(\frac{R_p}{R_{ref}}\right)^c\left(\frac{r}{R_p}\right)^a. \quad (13)$$

Note that if $R_p = R_{ref}$, Eq. (13) reduces to Eq. (11). Inserting our scaling factors for n_0 into Eq. (12), we obtain a scaled expression for $C(r)$,

$$C(r) = n_0\left(\frac{R_p}{R_{ref}}\right)^c\left(\frac{r}{R_p}\right)^a {d_{boulder}}^{-b}. \quad (14)$$

Using this we can convert the boulder CSFD to a secondary crater CSFD. We first make use of Eq. (6) to express fragment diameter as a function of secondary crater size:

$$D_f = k^{\frac{-1}{1-\beta}}\left(\frac{\delta}{\rho}\right)^{\frac{-1}{3(1-\beta)}} R_s^{\frac{1}{1-\beta}} r^{\frac{-\beta}{1-\beta}}. \quad (15)$$

Eqs. (14) and (15) can be inserted into Eq. (10), giving the secondary crater CSFD:

$$N_{>R_s}(R_p, r) = n_0 d_{boulder}^{-b} k^{\frac{-b}{1-\beta}}\left(\frac{\delta}{\rho}\right)^{\frac{-b}{3(1-\beta)}} R_{ref}^{-c} r^{a-\frac{b\beta}{1-\beta}} R_p^{c-a} R_s^{\frac{b}{1-\beta}}. \quad (16)$$

Eq. (9) contains $\frac{dN(R_s,r)}{dR_s}$, which is the secondary crater SFD at a distance r from the primary crater. This can be obtained from ((16) by differentiating with respect to R_s,

$$\left|\frac{dN(R_s,r)}{dR_s}\right| = n_0 d_{boulder}^{-b} k^{\frac{-b}{1-\beta}}\left(\frac{\delta}{\rho}\right)^{\frac{-b}{3(1-\beta)}} R_{ref}^{-c}\left|\frac{b}{1-\beta}\right| r^{a-\frac{b\beta}{1-\beta}} R_p^{c-a} R_s^{\frac{b}{1-\beta}-1}. \quad (17)$$

Now we can substitute Eq. (17) into Eq. (9) and obtain:

$$P = 1 - \exp\left[-\int_{\max\left(R_{min}, \frac{h}{2\alpha}\right)}^{R_{max}} c_1 R_p^{c-a} r^{a-\frac{\beta b}{1-\beta}}\left(R_s^{\frac{b}{1-\beta}+1} - \frac{h}{2\alpha} R_s^{\frac{b}{1-\beta}}\right) dR_s\right], \quad (18)$$

where $c_1 = \pi n_0 d_{boulder}^{-b} k^{\frac{-b}{1-\beta}} (\frac{\delta}{\rho})^{\frac{-b}{3(1-\beta)}} R_{ref}^{-c} |\frac{b}{1-\beta}|$. Eq. (18) is equivalent to Eq. (9), but with additional parameters (a, b, and c) that are constrainable from observations. Also, the secondary crater frequency distribution, $dN(R_s)/dR_s$, is now expressed in a term that depends on the size of a primary crater, the downrange distance of a rayed area, and the size-frequency distribution of ejecta fragments.

To integrate Eq. (18), we must first set upper and lower bounds on the size of secondary craters. We assume that the upper bound of secondary crater size is infinite and, because we are only interested in secondary craters that excavate bright material, the lower bound of secondary size is limited to the craters that excavate below $h/2\alpha$. Note that, when substituting our upper bound of infinity in for the integrated R_s terms, infinity appears in the numerator of multiple terms throughout the equation. In order to integrate this equation, the infinite crater size must be moved to the denominator, so that those terms become zero. To do so requires a constraint on b so that $b < -2(1-\beta)$. After integrating, we can simplify Eq. (18) into the probability that a surface is excavated to a depth of h. In other words, this P is the fraction of a given area that is excavated to a depth h, and is given as:

$$P = 1 - \exp\left[-c_2 R_p^{c-a} r^{a-\frac{\beta b}{1-\beta}}\left(\frac{h}{2\alpha}\right)^{2+\frac{b}{1-\beta}}\right], \quad (19)$$

where $c_2 = \frac{c_1}{[(1+\frac{b}{1-\beta})(2+\frac{b}{1-\beta})]}$.

From Eq. (19), we can solve for the relationship between the downrange distance (r) and the size of a primary crater (R_p). This equation can be solved to determine the distance at which the secondary craters no longer excavate a significant fraction of the surface to a depth equal to the space-weathered skin depth. This downrange distance r is the ray length R_r. We thus substitute R_r for r in Eq. (19) and obtain:

$$R_r = R_1 {R_p}^s, \quad (20)$$

where $R_1 = (\frac{h}{2\alpha})^{\frac{-2-b/(1-\beta)}{a-\beta b/(1-\beta)}} |\frac{\ln(1-P)}{-c_2}|^{\frac{1}{a-\beta b/(1-\beta)}}$, and $s = \frac{a-c}{a-\beta b/(1-\beta)}$. The term of R_p is equivalent to the R_p in Baldwin's empirical fit, Eq. (1). We note that both s and the exponent of $\ln(1-P)$ term share the same dominator, $a - \beta b/(1-\beta)$. The relationship $a = \beta b/(1-\beta)$ causes a degeneracy, which leads to the constraint $a \neq \beta b/(1-\beta)$.

The proportionality factor in front of R_p in Eq. (20), R_1, is equivalent to the proportional constant of the empirical fit to the ray length dependence on primary crater size from Eq. (2). We can see that this term in our study depends on the space-weathered skin depth (h), the secondary crater SFD and spatial density (defined using the parameters a, b, and c), and the fraction of a rayed surface (P) that is excavated to an excavation depth (h). The exponent term of R_p in Eq. (20), s, is suggested as 1.25 in Baldwin's empirical fit, yet this exponent is characterized by the three parameters of a, b, and c that are associated with the SFD of ejecta fragments. Our model contains a number of simplifying assumptions, and many of the parameters are individually poorly constrained. It is therefore necessary to discuss the uncertainties on the constraints of each variable in Eq. (20). In the next section, we will examine the physical meaning behind the parameters of our model.

4.2. Model uncertainties

Here we discuss each parameter in our analytical model and its uncertainty. We will elaborate on their physical meaning as well as the range of possible values, which are summarized in Table 3. In Section 4.3 we will examine combinations of parameters that match our empirical fit of the ray length vs. primary crater size relationship given in Eq. (2) and discuss their feasibility. The primary source of uncertainty in our model is the function that describes the spatial density of ejecta fragments (boulders) at the ray terminus given in Eq. (14).

4.2.1. Mean spatial density of boulders, "a"

Parameter a defines a power law index describing spatial boulder density as a function of landing distance. It is observed from a single crater observation on boulder count in Censorinus crater. There is spatial variability in boulder density, with some sparse regions (possibly indicating the avoidance zone) and denser regions which may be the beginnings of rays. To examine this variability, we fit a power-law function to the mean, 75th percentile, and maximum boulder counts (Fig. 6). Since this measurement is taken within the continuous ejecta blanket, there is an uncertainty of how boulder density varies beyond the continuous ejecta. However, for the purpose of this examination, we will assume that the spatial density follows the power law defined in Eq. (14).

4.2.2. Boulder density at rim of Censorinus, "n_0"

Parameter n_0 is the boulder density at the rim of Censorinus crater in units of number per km^2. This value, along with parameter a, controls the number of boulders at a given distance. It is calculated by fitting a power-law to boulder density as a function of distance (Fig. 6) and calculating the density at the crater rim. As rayed regions have much higher secondary crater densities, and therefore boulder densities, than neighboring ray-free regions,

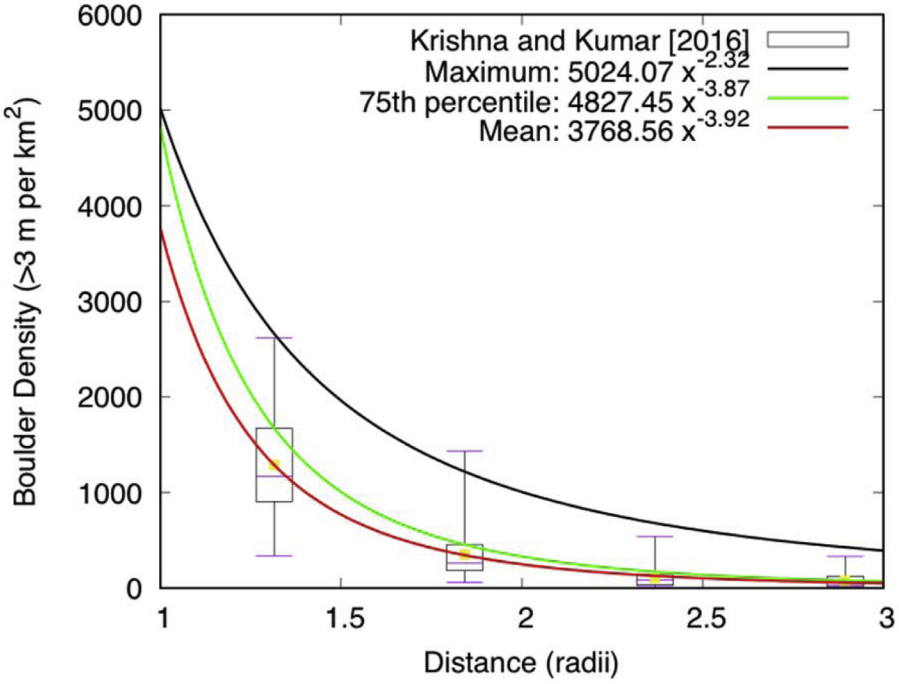

Fig. 6. Mean boulder density as a function of distance from the center of Censorinus crater. Note that distance is in terms of crater radii. The boxes represent boulder density measurements at the corresponding distance from Censorinus crater. We fit several power-laws to these data points in order to estimate how boulder density changes with distance. We use the power-law indices as a basis for our parameter *a*. The intercept of these curves is n_0, signifying the boulder density at the rim. Many regions surrounding Censorinus crater possess higher densities, possibly indicating rays. Data from Krishna and Kumar (2016).

we only consider densities at or above the average. This serves to eliminate any bias from boulder counts within ray-free regions.

*4.2.3. Ejecta fragment CSFD, "*b*"*

Parameter *b* is the power index associated with the power-law fit to boulder CSFD. The parameter *b* is a proxy for whether the ejecta has undergone a simple or complex fragmentation process, with less negative *b* values indicating simple and more negative values indicating complex (Hartmann, 1969; Kumar et al., 2014). A more negative value indicates that fragments are undergoing greater amounts of fracturing, leading to smaller fragment sizes. Values measured in Krishna and Kumar (2016) vary greatly, ranging from −1 to −7.6. More negative values were noted in distal regions, indicating reduced boulder sizes. Bart and Melosh (2010) measured values ranging from −3.0 to −5.5, while McEwen and Bierhaus (2006) suggest values from −2.9 to −4.6.

*4.2.4. Dependence on primary crater size, "*c*"*

Parameter *c* indicates the dependence on primary crater size. As the boulder density at a distance is correlated to the total number of boulders produced, one possible variable that links to the total production of boulders is the size of a primary crater. Bart and Melosh (2010) counted boulders >9 m in size for primary craters between >200 m and 41 km in diameter. In general, the number of boulders exterior to the crater increases with the size of a primary crater (Fig. 7). The relationship between the number of boulders and the crater size is evident in craters < 2 km, and it can be approximated by a power law with a power index of 1.12. For larger craters (4, 27, and 41 km), boulder number appears independent of crater size. This suggests that two different relationships, near-linear and independent, may be used in our model. We caution that the minimum observable boulder size in Bart and Melosh (2010), 9 m, is three times larger than in Krishna and Kumar (2016). It is uncertain whether the relationship between ejected boulder number and crater radius would change at higher resolutions.

The physical interpretation of our variable *c* is that it controls the number of boulders at the rim of the crater (n_0). This is the basis for allowing us to estimate the number of boulders at any given landing distance. The special case of $c = 1$ means that craters are self-similar, such that a crater's boulder population is linearly proportional to primary crater size. The special case of $c = 0$ means that the number of boulders is independent of the primary crater size.

4.2.5. Probability a surface being excavated to depth h*, "*P*"*

In order for a ray to be visible, some fraction of the surface area impacted by secondary fragments must excavated, emplacing bright, unweathered material onto the surface. The fraction of surface area can be thought of as a probability, and so parameter *P* is the required probability that the ejecta fragments excavate the surface to the space-weathered skin depth *h* in order for rays to be visible. It is uncertain what value of *P* is appropriate, but we can set plausible limits.

Consider two possible extreme values of *P*, either 0 or 1. If we were to set $P = 1$, this would be the case where rays would only be visible if the spatial density of ejecta fragments whose size was just big enough to excavate down to the skin depth *h* saturated the surface with bright unweathered secondary ejecta. If $P = 0$ were chosen instead, this would be the case where none of the surface needs to excavate down to the skin depth *h*. In such a case there would be no overturn of the surface, resulting in Eq. (20) equaling zero as well, meaning there is no ray.

As the length of a visible ray is subjective and dependent on image resolution, *P* should be dependent on resolution as well. In order for a ray to be visible, lower resolution images require a larger area of the surface to be excavated than higher resolution images would. Given this uncertainty, we will continue our analysis with the assumption that 50% of the surface must be excavated in order for a ray to be visible, so that $P = 0.50$.

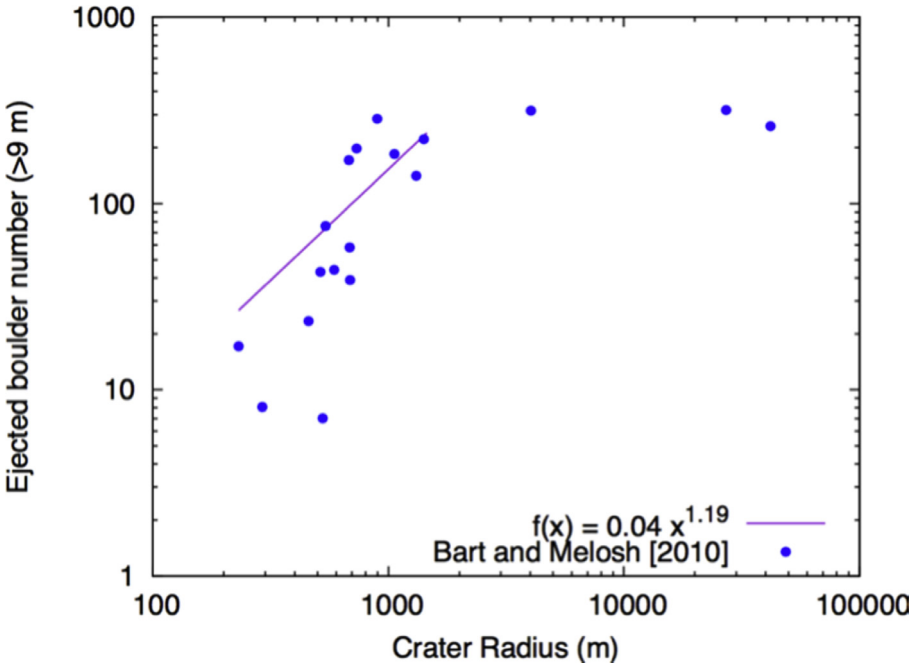

Fig. 7. Number of ejected boulders as a function of crater radius. We fit a power-law index of 1.19 for smaller craters, while there is no observed dependence for larger craters. This power-law index is our parameter *c*. Data from Bart and Melosh (2010).

4.3. Modeling results

To model the ray formation process, we approximate ejecta as a stream of boulders characterized by a size-frequency distribution (controlled by *b*, *c*, and n_0) and the density of boulders at a given landing distance (controlled by *a*). We want to know at what distance the majority of boulders will not be able to excavate beneath the mature soil layer. Past this distance, a few large boulders may occasionally excavate beneath this layer, but these will be isolated events and not considered part of the ray. In this section we will examine combinations of parameters, summarized in Fig. 8, and their fits to the observational data.

We begin with analyzing the power-law index term, *s*, in Eq. (20). We set *s* equal to 1.29, which is upper bound of the power-law index from our empirical fit (Eq. (2)). Several values of *c* are selected, ranging from 0 to 1.2. We use these *c* values to solve for values of *a* and *b* that result in $s = 1.27$. Solutions are plotted as solid black contours in Fig. 8, with each contour labeled with its respective *c* value. We see that smaller values of *c* can be satisfied by a wider range of *a* and *b* values, while large *c* values require higher magnitudes of *a*.

Next we analyze the proportionality factor, R_1, in Eq. (20). We set $R_1 = 6.59$, which is the proportionality factor from our empirical fit from Eq. (2). We then solve for skin-depth *h* across all values of *c*. Parameters *a* and *b* are constrained so that $s = 1.29$, as described in the preceding paragraph. Several *h* values are plotted as dashed contours in Fig. 8. The *c* contours (solid black lines) can be used to determine the *c* value along the *h* contour. Using the *c* contours and the position of the *h* contour, the *a* and *b* values needed for a specific skin-depth can be found. Intersections between the *c* and *h* contours provide model parameters that satisfy all components of the observational fit.

We now wish to use our model with a set of parameters provided in Fig. 8 to predict ray lengths over a wide range of primary craters (Fig. 9). We choose $h = 10$ *cm* and $c = 0$ so that $a = -4.5$ and $b = -5$, and set $P = 0.5$. We will also calculate ray length for other values of *h*, holding all other parameters constant.

As a validation of our model results we examined a section of a ray of Censorinus crater (Fig. 10). Our examined region is ~8 radii away from crater center. Using $a = -5$, $n_0 = 4827$ km^{-2}, $b = -4.5$, $c = 0$, and $P = 0.5$, our model predicts secondary craters with a diameter of ~1.34 m. This is near the resolution limit of LROC (~50 cm/px), with each secondary being less than 3 pixels in diameter. We see several larger secondaries (3–5 m in diameter), but not enough to saturate the area. Instead, much of the area is filled with either smaller secondaries or other bright ejecta.

While the model fits larger craters, the ray length distribution for small craters <100 m in radius do not fit well. Our ray formation model assumes that rays are largely composed of local material, rather than primary crater ejecta (Pieters et al., 1985). However, the observed ray lengths for two of the smallest craters (<5 m) are ~10 times longer than this model predicts. This suggests that the rays of small craters are not the result of secondary cratering and may be deposits of primary crater material. This motivates us to propose a different mechanism for ray formation for the smallest craters. Small crater ejecta are less energetic than large crater ejecta, and therefore distal ejecta from small craters may be too low in energy to excavate local material to depths sufficient to expose unweathered rocks.

In the low energy deposition regime, the ejecta fragments do not have enough mass or velocity to excavate below the skin layer. This implies that for the smallest craters, distal ejecta fragments do not form secondary craters. Instead, primary crater ejecta, which are unweathered, are deposited atop the surface. The ejecta may also slide along the surface, coming to a rest at some distance from the initial impact site used by our model (Runyon and Barnouin, 2016, 2014). This leads to rays that are longer than predicted by our ejecta model, Eq. (2). If this hypothesis is correct, then we can use our observations of crater rays to estimate where this low energy regime occurs. In Fig. 9 we have plotted several contours of ejection/landing velocity, which shows that the anomalously long crater rays appear to approximately follow the 10 m/s contour. At greater speeds, rays follow the trend predicted by our secondary crater scaling model. This suggests that the minimum velocity required to produce a secondary crater is ~10 m/s, which

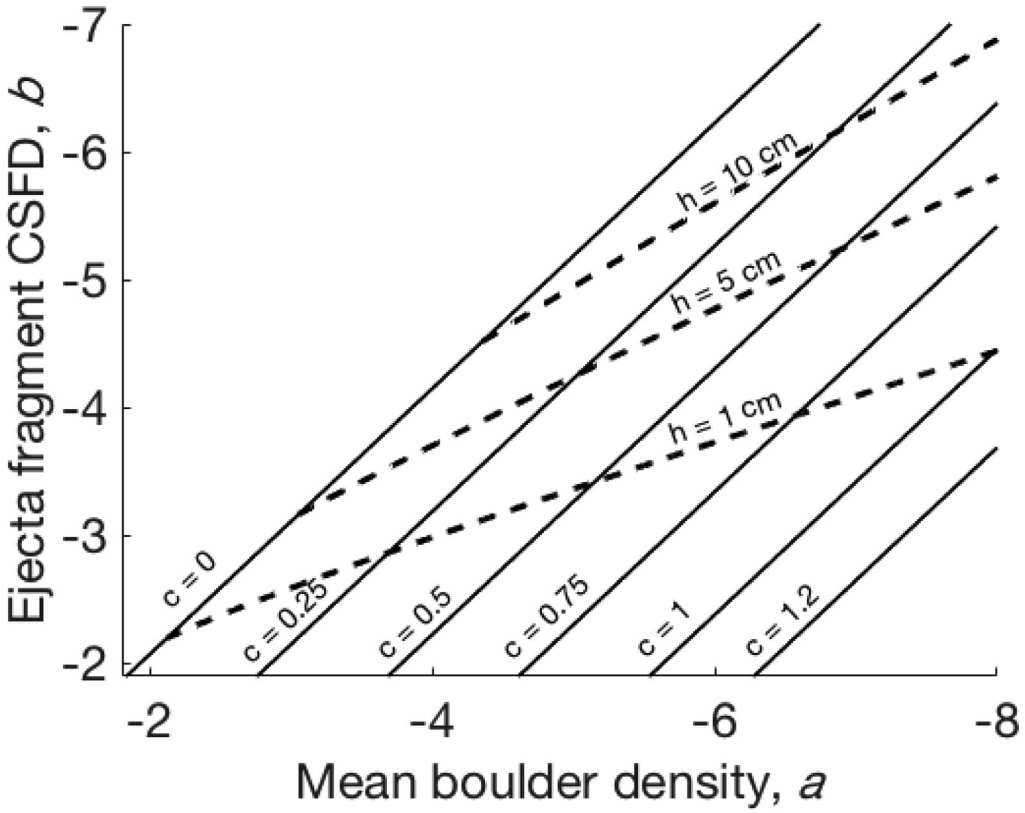

Fig. 8. Summary of model parameters needed to match the observational data (see Table 3 for a summary of model parameters). Axes are constrained to the ranges of a (mean spatial density of boulders) and b (ejecta fragment CSFD) observed by Krishna and Kumar (2016). The solid black lines are contours of c (dependence on primary crater size) values that satisfy $s = 1.27$, which is the upper bound of the power-law index of the empirical fit to the ray length measurements of this study. Dashed contours represent the space-weathered skin depth value h that satisfy $R_1 = 6.59$, which is the proportionality factor of the empirical fit of the ray length measurements. The points at which the skin-depth contours intersect the c contours give values that satisfy all components of the empirical fit.

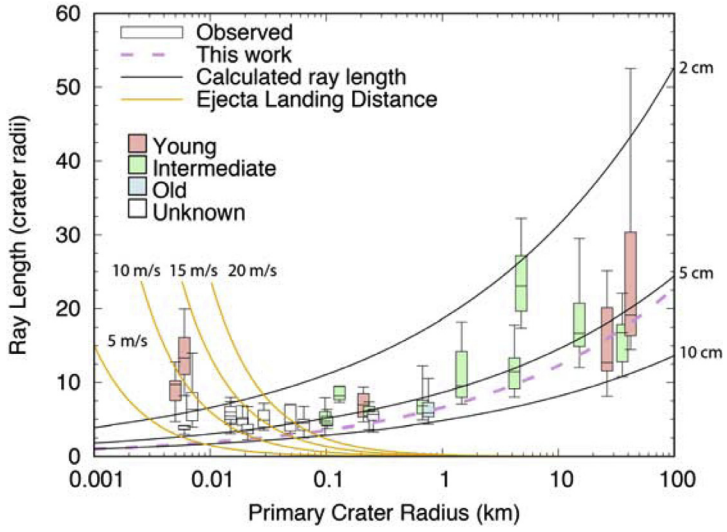

Fig. 9. Similar to Fig. 5, with the addition of our secondary crater hypothesis model, black contours that represent the predicted ray length for different depths of the dark lunar skin. The following parameter values were used: $a = -4.5$, $b = -5$, $c = 0$, $P = 0.50$. Also plotted are the landing distances of ejecta that are ejected with the given speed (orange contours). (For interpretation of the references to color in this figure legend, the reader is referred to the web version of this article.)

is significantly lower than the sound speed in lunar soil of 108 m/s (Latham et al., 1970). It is also significantly smaller than the proposed minimum velocity for secondary crater formation of 150–250 m/s inferred for icy satellites (Bierhaus et al., 2012). Due to this discrepancy in necessary velocities, an alternative mechanism may be that ejecta impacting at greater than 10 m/s are able to bury into the mature soil layer without excavating beneath it. At such low impact speeds, the impactor is likely to stay intact (Bland et al., 2008, 2001; McDermott et al., 2016; Nagaoka et al., 2014). Such a low impact velocity is unlikely to trigger excavation (Melosh, 1985). As a result, we have an intact fragment hitting the surface and possibly burying itself without triggering any excavation of underlying material. This will keep the surface free of bright material, preventing ray formation.

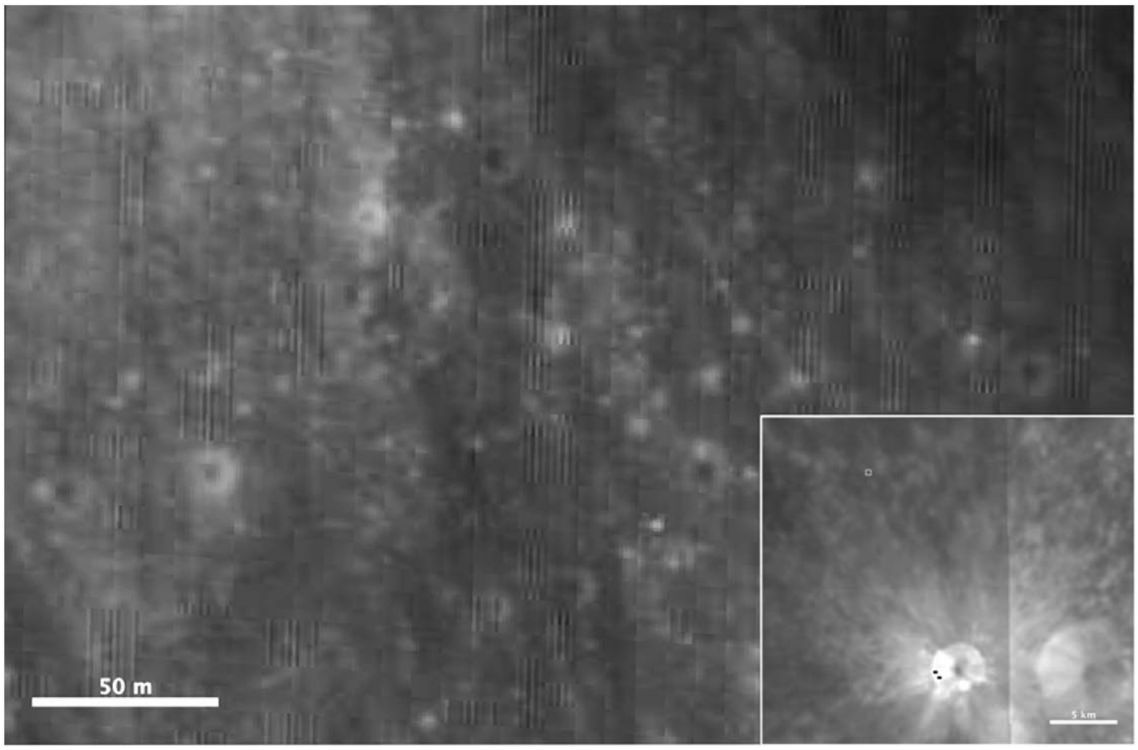

Fig. 10. A region 16 km (~8 radii) away from Censorinus crater (red point in insert). Our ray model predicts secondary craters with a diameter of ~1.34 m at this distance. This is approaching the resolution limit of LROC, with each crater being less than 3 pixels in diameter. We see several larger secondaries, but not enough to saturate the area. Instead, the area is saturated with either smaller secondaries or other bright ejecta. (For interpretation of the references to color in this figure legend, the reader is referred to the web version of this article.)

4.4. Analytical model limitations

Throughout the derivation of the analytical model in Section 4.1, several simplifying assumptions were made. Despite these assumptions, the model is still multi-variable and fairly complex. These assumptions and poorly constrained variables create significant limitations on the accuracy and usefulness of such a model. Still, the derivation serves as a useful exploration of the physical properties behind ray formation and serves as a starting point in furthering our understanding of rays and secondary craters.

The analytical model uses Poisson statistics to determine the spatial coverage of secondary craters. While Poisson statistics has been used to describe the spatial coverage of circles (Garwood, 1947), but it may not be accurate for craters within rays. Secondary craters outside of the continuous ejecta blanket are not randomly distributed. Some mechanism, possibly inelastic collisions between ejecta particles (Kadono et al., 2015), organizes ejecta to form high spatial density clusters of secondary craters.

The model contains four poorly constrained variables describing ejecta behavior and one arbitrarily chosen variable, P. While there have been many studies that attempt to constrain ejecta behavior (Bart and Melosh, 2010; Clegg-Watkins et al., 2016; Krishna and Kumar, 2016; Vickery, 1987), an analytical solution does not yet exist. Numerical models are beginning to accurately describe fragment size and velocity (Head et al., 2002; Melosh et al., 2017, 1992), but there are still many unknowns, such as the effect of target strength (Dundas et al., 2010; Prieur et al., 2017; van der Bogert et al., 2017). Such a large number of poorly constrained variables leads to the existence of multiple parameter sets that match the observational data (Fig. 8). The existence of multiple valid parameter sets makes it difficult to use the analytical model for ray length predictions. However, the model does serve as an investigation into the physical processes that determine ray length.

Local variations in terrain, both near the primary crater and in distal secondary fields, were not accounted for in the model. Variations in target material, such as rock strength and pre-existing damage, may affect ejection speeds and fragment sizes (Head et al., 2002). Variations in the distal ejecta field, such as hills, rock strength, and local skin depth, will affect the formation and visibility of secondary craters. Unfortunately, local terrain variation is too variable and detailed to include in an analytical model. However, numerical models may be able to account for these features (Shuvalov, 2012).

Our ejecta model is constrained to a 45° ejection and impact angle. This was done in order to simplify the conversion between distance and ejection velocity (Eq. (5)). While 45° ejection angle is a standard ejection angle from the Maxwell Z-model (Maxwell and Seifert, 1974), ejection angles tend to vary over 35–55° (Cintala et al., 1999; Richardson et al., 2007).

Future observations and experiments will help further our understanding of the ray process and constrain any variables that may appear in analytical models. Most lacking is our understanding of the impact ejecta fragment size distribution. Studies have attempted to constrain their number, sizes, and velocities (Bart and Melosh, 2010; Head et al., 2002; Vickery, 1987), but there is not yet an analytical model or well-constrained distribution (Chappaz et al., 2012). Impact experiments on secondary craters are needed to constrain their excavation depths, as their crater depth-to-diameter ratios vary from primary craters. Finally, further study is needed on the terminations of crater rays. Our model predicts secondary craters at below LROC resolutions, so it is difficult to verify the process that causes a ray to terminate. Further high-resolution images or ground samples are needed to constrain that process.

Table 3
Summary of model parameters.

Parameter	Description	Values	Source
a	Power law index of ejecta fragment spatial density vs. downrange distance relationship	−2.3 to −6.5	Krishna and Kumar (2016)
n_0	Boulder density per km^2 at the rim of reference crater (Censorinus crater)	3768–5024	Krishna and Kumar (2016)
b	Power law index of ejecta fragment CSFD	−1 to −7.6	Krishna and Kumar (2016)
		−3 to −5.5	Bart and Melosh (2010)
c	Power law index of ejecta fragment spatial density vs. primary crater size relationship	0–1.2	Bart and Melosh (2010)
P	Required probability that the ejecta fragments excavate the surface to space-weathered skin depth h in order for rays to be visible	0–1	This study

5. Discussion

5.1. Ray formation

Our ray model results lead us to define three regimes, all of which are part of a ray, whether visible or not: 1) Low Energy Deposition, in which ejecta land at low enough velocity that they do not vertically mix with the target, instead ejecta are simply deposited atop the surface; (2) High Energy, Deep Excavation, where ejecta have high enough velocities and masses to excavate unweathered material from below the weathered/mature layer; (3) High Energy, Shallow Excavation, where at the furthest distances, ejecta are small enough that they do not excavate below the weathered layer (Fig. 11). The high energy, deep excavation regime appears to be the regime in which most visible rays exist. The ejecta in this regime have enough velocity and mass to excavate below the skin layer, which brings bright, unweathered material to the surface. As distance from the primary crater increases, so do ejecta velocities. However, the ejecta masses decrease. As a result, secondary crater size and excavation depth decreases. Eventually the secondary craters are too small to excavate below the skin depth. It is at this point that the visible ray ends and the third regime begins. In the high energy, shallow excavation regime, secondary craters are no longer capable of excavating fresh material to the surface. Instead, they simply overturn already weathered material. These secondary craters and their ejecta blankets are thus indistinguishable from the lunar background. So while there is still a small amount of fresh primary crater ejecta, the fresh material is diluted by the weathered material, and thus no rays are visible. This regime is similar to the distal low reflectance zone (DLRZ) found by Robinson et al. (2015) and Speyerer et al. (2016). In this zone, only the upper mature layer is reworked, leading to increased surface roughness but not increased albedo.

While ray lengths follow the expected trend, there does not appear to be a discernable relationship between OMAT and ray length in the larger craters (>600 m in radius). All craters in this size category follow the general trend of increasing relative length as a function of primary size. Smaller craters, however, do appear to exhibit a relationship between OMAT and ray length: the youngest, freshest craters are the longest, while the oldest craters are the shortest, with middle-aged craters in-between (Fig. 8). It is likely that surfaces affected by smaller craters are disturbed to a lesser degree than surfaces surrounding larger craters. A less disturbed surface should either have lower OMAT values than a highly disturbed surface or equivalent OMAT values, but will weather more quickly due to the smaller volume of immature material. These lightly disturbed surfaces would require less weathering and time in order to reach full maturity. This trend is similar to the size bias discussed by Grier et al. (2001, 2000), who noted that smaller craters age more quickly than larger craters. Compositional rays, such as those of Lichtenberg (Hawke et al., 2004), do not degrade with time. Instead, they remain at their initial length. While they do not give any information about how space-weathering affects ray length, they do give a relatively accurate image of the initial ejecta emplacement. However, this method of ray formation is completely separate from the method proposed in this study. Instead of requiring the excavation of subsurface immature material, compositional rays form from the emplacement of primary crater ejecta atop the surface. These rays are visible because of compositional differences between highlands and mare materials. For this reason, we do not consider compositional ray data in our observational fit or analytical model.

Assuming that the space-weathered layer on the Moon sets a limit on the extent of visible ray system for kilometer-sized craters, the extent of lunar rays will increase as the thickness of the dark skin layer decreases. As distance from the primary crater increases,

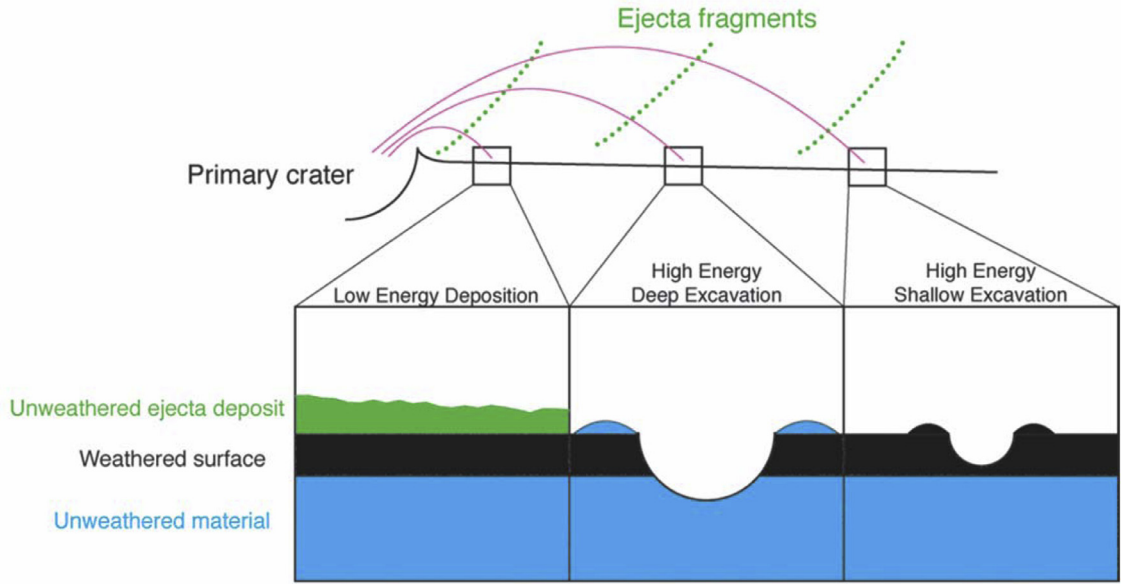

Fig. 11. Effects of ejecta fragment impacts on the lunar surface. There are three regimes based on energy and excavation depth. 1) Low energy deposition: Ejecta that land at low enough velocity that they do not vertically mix with the target. Ejecta from the primary crater are simply deposited atop the surface. This can occur in proximal ejecta blankets as well as distal rays of very small craters. 2) High energy deep excavation: At this distance, ejecta have high enough velocities and masses to excavate unweathered material from below the weathered/mature layer. It is in this region that rays are formed. 3) High energy shallow excavation: At the furthest distances, ejecta are small enough that they do not excavate below the weathered layer. No fresh material is brought to the surface and rays are not visible.

we expect to see smaller ejecta fragments. A thinner skin layer allows those smaller fragments to easily excavate fresh material from beneath, and as a result a longer visible ray is expected. There may be variability in skin layer thickness, leading to a dependence on the local surface where a ray forms. For example, a less disturbed surface has time to develop a deeper skin layer, while a nearby surface may have been resurfaced by fresh ejecta from a local cratering event. This discrepancy in skin-depths could contribute to the varying ray lengths we observe.

The extent of an individual ray system may be spatially variable, but a general trend of increasing length with the size of its primary crater is observed. Using observational constraints, our parameterized model can explain an overall trend of ray length seen in Baldwin's empirical formula and our mapping data. The relationship between the fragment SFD and the Baldwin's empirical formula suggests a unique process occurring in the distal ejecta regime. It appears that the fragment SFD in the distal ejecta is likely governed by a random process. The overall increasing trend in ray lengths is best explained by the total number of boulders being independent of the size of a primary crater (the *c* parameter in our model). This is a surprising result, as one would expect the total number of boulders to scale with primary crater size. However, observational data from Bart and Melosh (2010) suggest that, for larger craters, there is not a relationship between the two (Fig. 7). This may have implications for the fragmentation and ejection of large boulders, but more study is required. Further boulder counts for a wide range of crater sizes or numerical modeling will constrain this relationship further. The trend of increasing relative length with increasing primary crater radius suggests that an equivalent-sized secondary will be created further away for a larger crater. For example, given craters A and B, if B is twice as large as A, B will produce the same sized secondaries at more than twice the distance that A does. This non-linear scaling is demonstrated by our secondary crater scaling model (Fig. 9). Each contour represents the distance at which a certain sized secondary crater is produced.

An analytical or numerical model that properly describes the ray process is important for determining how material is transported across the planetary surface (Huang et al., 2017) and for evaluating possible landing sites for future missions (Haskin et al., 2003). While observational constraints do lead to parameter sets that satisfy the observational measurements of our study, multiple such parameter sets exist. As such, the analytical model does not serve to constrain these variables further, nor does it currently serve as a necessarily predictor of ray lengths (although it is able to match observational data). Instead, it better serves to explore the physical process that determines ray length. Future observational constraints, such as those described at the end of Section 4.4, may make such an analytical model more useful.

5.2. Comparison of lunar and Martian rays

Lunar rays, when compared to their Martian counterparts, are relatively short, despite being formed by the same secondary cratering process Quantin et al., 2016). Zunil and Tomini craters, 5 and 3.7 km in radius, respectively, both have rays reaching out to 180 radii (Tornabene et al., 2006). A ray of an equivalent-diameter crater on the Moon, designated "SE of Ritz," has been measured at ~37 radii. Given Mars's higher gravity and atmosphere, the ballistic ranges of ejecta are shorter, and thus one would expect shorter rays. However, this is clearly not the case. As shown between Eqs. (4) and ((6) of our model, the gravity term cancels out and is absent from the final model. So while ballistic range is indeed shorter on Mars than the Moon, it is not a factor in our analytical model and doesn't affect overall ray lengths. The atmosphere of Mars does not greatly affect fragments larger than 14–20 cm (Artemieva and Ivanov, 2004), which is smaller than the majority of secondary forming fragments.

There are several key differences between known Martian ray systems and lunar ray systems that may explain the difference in measured lengths. Mars's surface is weathered by aeolian processes acting on short timescales, while the Moon experiences space-weathering by micrometeorite impacts and the solar wind.

Zunil crater is estimated to be less than 5 Ma (McEwen et al., 2005), while its lunar counterpart, "SE of Ritz", is estimated to be 109–782 Ma, based on our OMAT measurements. Martian ray systems appear to form from impacts in cohesive rock, such as lava flows (Tornabene et al., 2006), while lunar rays can form from impacts into loose rock or regolith. Further, Martian rays only appear on areas with a thin layer of dust (McEwen et al., 2005; Preblich et al., 2007). Only 10% of the Martian surface is covered in thin dust, with the rest covered in a much thicker layer (Preblich et al., 2007). It may be easier to disturb this thin layer of dust than it is to excavate below the lunar skin, leading to long Martian rays that do not depend on secondary cratering, but rather simple surface disturbances. The most probable explanation is a difference in ray definition: Martian rays are thought to largely be the result of thermal differences between local and ejected material, with rays rarely showing albedo differences (Tornabene et al., 2006), whereas most lunar rays, by definition, have distinct albedo differences. If our proposed third ray regime, high energy shallow excavation, was measured, rays may extend to comparable distances. Robinson et al. (2015) measured surface properties and found disturbed surfaces at 50 radii, with some isolated splotches of material reaching ~3000 radii. Hayne et al. (2017) developed a thermal inertia map of the Moon using Diviner data and found that rays are prominent high-inertia features. Similar to Tornabene et al. (2006), this new data set could be used to measure ray length in non-visible spectrums.

6. Conclusions

This study mapped 27 lunar craters ranging from 10 m to 84 km in diameter and measured the number of rays, ray lengths, and OMAT of each. We developed a new empirical power-law relationship between ray length and primary crater size. This new fit is slightly steeper than found by Baldwin (1963). To explain the observational data, we developed an analytical model describing how secondary crater size should change with distance. Our model allows for ray lengths to be predicted for kilometer-sized primary craters. Analysis of our model produces combinations of parameters to match the empirical fit of our study (Fig. 8). This provides a theoretical constraint of ejecta fragment SFDs and fragment densities. We also found that eventually secondary craters become too small to excavate bright, fresh material from beneath the dark lunar "skin." This transition from bright to dark excavated material can be thought of as the end of the visible ray. This secondary crater model was then used to observe how the composition of a ray changes with distance from the primary crater. For larger primary craters, the ejecta become insignificant past the continuous ejecta blanket. Further out, most ray material is locally excavated. On the other hand, rays associated with smaller primary craters seem to be composed of ejecta, leading them to be longer than would be expected based on the empirical relationship. We thus define three regions of ray formation: *low-energy deposition*, in which primary crater ejecta are deposited on the surface with little excavation, *high-energy deep excavation*, in which ejecta excavated fresh material from below the lunar surface, and *high-energy shallow excavation*, in which ejecta simply overturn the dark lunar soil and does not produce a visible ray.

Acknowledgments

Any data, including custom maps, may be obtained from the corresponding author (elliot26@purdue.edu). LROC and OMAT images are available through PDS and JMARS. The authors would like to thank Gareth Collins and Colin Dundas for their help in strengthening an early version of this manuscript. The authors wish to thank two anyonymous reviewers for their detailed reviews and helpful comments. This work is supported by the NASA Solar System Workings program (grant number NNX15AL41G).

References

Anderson, J.L.B., Schultz, P.H., 2003. Asymmetry of ejecta flow during oblique impacts using three-dimensional particle image velocimetry. J. Geophys. Res. 108. doi:10.1029/2003JE002075.

Artemieva, N., Ivanov, B., 2004. Launch of Martian meteorites in oblique impacts. Icarus 171, 84–101. doi:10.1016/j.icarus.2004.05.003.

Baldwin, R.B., 1963. The Measure of the Moon, first ed. University of Chicago, Chicago.

Bart, G.D., Melosh, H.J., 2010. Distributions of boulders ejected from lunar craters. Icarus 209, 337–357. doi:10.1016/j.icarus.2010.05.023.

Bierhaus, E.B., Dones, L., Alvarellos, J.L., Zahnle, K., 2012. The role of ejecta in the small crater populations on the mid-sized saturnian satellites. Icarus 218, 602–621. doi:10.1016/j.icarus.2011.12.011.

Bland, P.A., Artemieva, N.A., Collins, G.S., Bottke, W.F., Bussey, D.B.J., Joy, K.H., 2008. Asteroids on the moon: projectile survival during low velocity impact. Lunar and Planetary Science Conference XXXIX Abstract #2045.

Bland, P.A., Cintala, M.J., Horz, F., Cressey, G., 2001. Survivability of meteorite projecticles - results from impact experiments. Lunar and Planetary Science XXXII Abstract #1764.

Borg, J., Comstock, G.M., Langevin, Y., Maurette, M., Jouffrey, B., Jouret, C., 1976. A Monte Carlo model for the exposure history of lunar dust grains in the ancient solar wind. Earth Planet. Sci. Lett. 29, 161–174. doi:10.1016/0012-821X(76)90036-4.

Bowman-Cisneros, E., Isbell, C., 2008. LROC RDR Data Products Software Interface Specification, pp. 1–38 Reviewed by.

Burko, L.M., Price, R.H., 2005. Ballistic trajectory: parabola, ellipse, or what? Am. J. Phys. 73, 516–520.

Cassidy, W., Hapke, B., 1975. Effects of darkening processes on surfaces of airless bodies. Icarus 25, 371–383.

Chappaz, L., Melosh, H.J., Vaquero, M., Howell, K.C., 2012. Transfer of impact ejecta material from the surface of Mars to Phobos and Deimos. Adv. Astronaut. Sci. 143, 1627–1646. doi:10.1089/ast.2012.0942.

Cintala, M.J., Berthoud, L., Hörz, F., 1999. Ejection–velocity distributions from impacts into coarse–grained sand. Meteorit. Planet. Sci. 34, 605–623. doi:10.1111/j.1945-5100.1999.tb01367.x.

Clegg-Watkins, R.N., Jolliff, B.L., Lawrence, S.J., 2016. Frequency-range distribution of boulders around cone crater: relevance to landing site hazard avoidance. Annual Meeting of the Lunar Exploration Analysis Group Abstract #5017 doi:10.1038/ngeo2252.

Dickenshield, S., Anwar, S., Noss, D., Hagee, W., Carter, S., 2015. JMARS-easy visualization and analysis of planetary remote sensing data. 2nd Planetary Data Workshop.

Dundas, C.M., Keszthelyi, L.P., Bray, V.J., McEwen, A.S., 2010. Role of material properties in the cratering record of young platy-ridged lava on Mars. Geophys. Res. Lett. 37. doi:10.1029/2010GL042869.

Dundas, C.M., McEwen, A.S., 2007. Rays and secondary craters of Tycho. Icarus 186, 31–40. doi:10.1016/j.icarus.2006.08.011.

Elbeshausen, D., Wünnemann, K., Collins, G.S., 2013. The transition from circular to elliptical impact craters. J. Geophys. Res. Planets 118, 2295–2309. doi:10.1002/2013JE004477.

Garwood, F., 1947. The variance of the overlap of geometrical figures with reference to a bombing problem. Biometrika 34, 1–17.

Gault, D.E., Wedekind, J.A., 1978. Experimental studies of oblique impact. In: Proceedings of Lunar Science Conference 9th, pp. 3843–3875.

Gault, E.D., Horz, F., Brownlee, E.D., Hartung, B.J., 1974. Mixing of the lunar regolith. Proceedings of the Fifth Lunar Conference 3, 2365–2386.

Grier, J.A., McEwen, A.S., Lucey, P.G., Milazzo, M., Strom, R.G., 2001. Optical maturity of ejecta from large rayed lunar craters. J. Geophys. Res. 106, 32847. doi:10.1029/1999JE001160.

Grier, J.A., McEwen, A.S., Milazzo, M., Hester, J.A., Lucey, P.G., 2000. The optical maturity of the ejecta of small bright rayed lunar craters. Lunar Planet. Sci. XXXI #1950.

Haiken, G.H., Vaniman, D.T., French, B.M., 1991. Lunar Sourcebook. Cambridge University Press.

Hapke, B., 1973. Darkening of silicate rock powders by solar wind sputtering. Moon 7, 342–355.

Hartmann, W.K., 1969. Terrestrial, lunar, and interplanetary rock fragmentation. Icarus 10, 201–213. doi:10.1016/0019-1035(69)90022-0.

Haskin, L.A., Moss, B.E., Mckinnon, W.B., 2003. On estimating contributions of basin ejecta to regolith deposits at lunar sites. Meteorit. Planet. Sci. 38, 13–33.

Hawke, B.R., Blewett, D.T., Lucey, P.G., Smith, G.A., Bell, J.F., Campbell, B.A., Robinson, M.S., 2004. The origin of lunar crater rays. Icarus 170, 1–16. doi:10.1016/j.icarus.2004.02.013.

Hawke, B.R., Giguere, T.A., Gaddis, L.R., Campbell, B.A., Blewett, D.T., Boyce, J.M., Gillis-Davis, J.J., Lucey, P.G., Peterson, C.A., Robinson, M.S., Smith, G.A., 2008. The origin of copernicus rays: implications for the calibration of the lunar stratigraphic column. Lunar and Planetary Science Conference XXXIX Abstract #1092.

Hawke, B.R., Giguere, T.A., Gaddis, L.R., Campbell, B.A., Blewett, D.T., Boyce, J.M., Gillis-Davis, J.J., Lucey, P.G., Peterson, C.A., Robinson, M.S., Smith, G.A., 2007. Remote sensing studies of copernicus rays: implications for the Copernican-Eratosthenian boundary. Lunar and Planetary Science XXXVIII Abstract #1133.

Hayne, P.O., Bandfield, J.L., Siegler, M.A., Vasavada, A.R., Ghent, R.R., Williams, J.P., Greenhagen, B.T., Aharonson, O., Elder, C.M., Lucey, P.G., Paige, D.A., 2017. Global Regolith Thermophysical Properties of the Moon from the diviner lunar radiometer experiment. J. Geophys. Res. Planets 2371–2400. doi:10.1002/2017JE005387.

Head, J.N., Melosh, H.J., Ivanov, B.A., 2002. Martian meteorite launch: high-speed ejecta from small craters. Science 298 (80), 1752–1756. doi:10.1126/science.1077483.

Herrick, R.R., Forsberg-Taylor, N.K., 2003. The shape and appearance of craters formed by oblique impact on the Moon and Venus. Meteorit. Planet. Sci. 38, 1551–1578. doi:10.1111/j.1945-5100.2003.tb00001.x.

Hiesinger, H., Van Der Bogert, C.H., Pasckert, J.H., Funcke, L., Giacomini, L., Ostrach, L.R., Robinson, M.S., 2012. How old are young lunar craters? J. Geophys. Res. E Planets 117, 1–15. doi:10.1029/2011JE003935.

Huang, Y.-H., Minton, D.A., Hirabayashi, M., Elliott, J.R., Richardson, J.E., Fassett, C.I., Zellner, N.E.B., 2017. Impact-generated material transport on the Moon. J. Geophys. Res. Planets.

Kadono, T., Suzuki, A.I., Wada, K., Mitani, N.K., Yamamoto, S., Arakawa, M., Sugita, S., Haruyama, J., Nakamura, A.M., 2015. Crater-ray formation by impact-induced ejecta particles. Icarus 250, 215–221.

Krishna, N., Kumar, P.S., 2016. Impact spallation processes on the Moon: a case study from the size and shape analysis of ejecta boulders and secondary craters of Censorinus crater. Icarus 264, 274–299. doi:10.1016/j.icarus.2015.09.033.

Krüger, T., van der Bogert, C.H., Hiesinger, H., 2016. Geomorphologic mapping of the lunar crater Tycho and its impact melt deposits. Icarus 273, 164–181. doi:10.1016/j.icarus.2016.02.018.

Kuiper, G.P., Arthur, D.W.G., Moore, E., Tapscott, J.W., Whitaker, E.A., 1960. Photographic Lunar Atlas Based on the Photographs Taken at the Mount Wilson, Lick, Pic du Midi, McDonald and Yerkes Observatories. The University of Chicago Press, Chicago, IL.

Kumar, P.S., Lakshmi, K.J.P., Krishna, N., Menon, R., Sruthi, U., Keerthi, V., Kumar, A.S., Mysaiah, D., Seshunarayana, T., Sen, M.K., 2014. Impact fragmentation of lonar crater, India: implications for impact cratering processes in basalt. J. Geophys. Res. Planets 119, 2029–2059. doi:10.1002/2014JE004685.

Latham, G.V, Ewing, M., Press, F., Sutton, G., Dorman, J., Toksöz, N., Wiggins, R., Derr, J., Duennebier, F., 1970. Passive seismic experiment. Science 167 (80), 455–457.

Lemelin, M., Lucey, P.G., Gaddis, L.R., Hare, T., Ohtake, M., 2016. Global map products from the Kaguya Multipand Imager at 512 PPD: Minearls, FeO, and OMAT. Lunar and Planetary Science Conference XLVII Abstract #2994 doi:10.1038/ngeo2474.

Lucey, P.G., Blewett, D.T., Taylor, G.J., Hawke, B.R., 2000. Imaging of lunar surface maturity. J. Geophys. Res. Planets 105, 20377–20386. doi:10.1029/1999JE001110.

Maxwell, D., Seifert, K., 1974. Modeling of Cratering, Close-in Displacements, and Ejecta. Technical Report Def. Nucl. Agency, Washington, DC.

McDermott, K.H., Price, M.C., Cole, M., Burchell, M.J., 2016. Survivability of copper projectiles during hypervelocity impacts in porous ice: a laboratory investigation of the survivability of projectiles impacting comets or other bodies. Icarus 268, 102–117. doi:10.1016/j.icarus.2015.12.037.

McEwen, A.S., Bierhaus, E.B., 2006. The importance of secondary cratering to age constraints on planetary surfaces. Annu. Rev. Earth Planet. Sci. 34, 535–567. doi:10.1146/annurev.earth.34.031405.125018.

McEwen, A.S., Preblich, B.S., Turtle, E.P., Artemieva, N.A., Golombek, M.P., Hurst, M., Kirk, R.L., Burr, D.M., Christensen, P.R., 2005. The rayed crater Zunil and interpretations of small impact craters on Mars. Icarus 176, 351–381. doi:10.1016/j.icarus.2005.02.009.

Melosh, H.J., 1985. Impact cratering mechanics: Relationship between the shock wave and excavation flow. Icarus 62, 339–343. doi:10.1016/0019-1035(85)90129-0.

Melosh, H.J., Johnson, B.C., Bowling, T.J., 2017. Impact spall and fragmentation by near-surface stress wave interactions. 48th Lunar and Planetary Science Conference.

Melosh, H.J., Ryan, E.V., Asphaug, E., 1992. Dynamic fragmentation in impacts: hydrocode simulation of laboratory impacts. J. Geophys. Res. 97, 14735–14759. doi:10.1029/92JE01632.

Moore, H.J., Hodges, C.A., Scott, D.H., 1974. Multiringed basins-illustrated by Orientale and associated features. In: Proceedings of the Fifth Lunar Conference, pp. 71–100.

Murphy, T.W., Adelberger, E.G., Battat, J.B.R., Hoyle, C.D., Johnson, N.H., McMillan, R.J., Michelsen, E.L., Stubbs, C.W., Swanson, H.E., 2010. Laser ranging to the lost Lunokhod∼1 reflector. Icarus doi:10.1016/j.icarus.2010.11.010.

Nagaoka, H., Takasawa, S., Nakamura, A.M., Sangen, K., 2014. Degree of impactor fragmentation under collision with a regolith surface-laboratory impact experiments of rock projectiles. Meteorit. Planet. Sci. 49, 69–79. doi:10.1111/maps.12126.

Neish, C.D., Blewett, D.T., Harmon, J.K., Coman, E.I., Cahill, J.T.S., Ernst, C.M., 2013. A comparison of rayed craters on the moon and mercury. J. Geophys. Res. Planets 118, 2247–2261. doi:10.1002/jgre.20166.

Pieters, C.M., Adams, J.B., Smith, M.O., Mouginis-Mark, P.J., Zisk, S.H., 1985. The nature of crater rays-the Copernicus example. J. Geophys. Res. 90, 393–413. doi:10.1029/JB090iB14p12393.

Pieters, C.M., Noble, S.K., 2016. Space weathering on airless bodies. J. Geophys. Res. Planets 121, 1865–1884. doi:10.1002/2016JE005128.Received.

Pieters, C.M., Taylor, L.A., Noble, S.K., Keller, L.P., Hapke, B.W., Morris, R.V, Allen, C.C., McKay, D.S., Wentworth, S.J., 2000. Space weathering on airless bodies: resolving a mystery with lunar samples. Meteorit. Planet. Sci. doi:10.1111/j.1945-5100.2000.tb01496.x.

Preblich, B.S., McEwen, A.S., Studer, D.M., 2007. Mapping rays and secondary craters from the Martian crater Zunil. J. Geophys. Res. Planets 112, 1–18. doi:10.1029/2006JE002817.

Prieur, N.C., Rolf, T., Luther, R., Wünnemann, K., Xiao, Z., Werner, S.C., 2017. The effect of target properties on transient crater scaling for simple craters. J. Geophys. Res. Planets 122, 1704–1726. doi:10.1002/2017JE005283.

Quantin, C., Popova, O., Hartmann, W.K., Werner, S.C., 2016. Young Martian crater Gratteri and its secondary craters. J. Geophys. Res. Planets 121, 1118–1140. doi:10.1002/2015JE004864.

Richardson, J.E., 2011. Modeling impact ejecta plume evolution: a comparison to laboratory studies. J. Geophys. Res. Planets 116, 1–16. doi:10.1029/2011JE003844.

Richardson, J.E., Melosh, H.J., Lisse, C.M., Carcich, B., 2007. A ballistics analysis of the deep impact ejecta plume : determining comet tempel 1's gravity, mass, and density. Icarus 191, 176–209. doi:10.1016/j.icarus.2007.08.033.

Robinson, M.S., Boyd, A.K., Denevi, B.W., Lawrence, S.J., McEwen, A.S., Moser, D.E., Povilaitis, R.Z., Stelling, R.W., Suggs, R.M., Thompson, S.D., Wagner, R.V., 2015. New crater on the Moon and a swarm of secondaries. Icarus 252. doi:10.1016/j.icarus.2015.01.019.

Robinson, M.S., Brylow, S.M., Tschimmel, M., Humm, D., Lawrence, S.J., Thomas, P.C., Denevi, B.W., Bowman-Cisneros, E., Zerr, J., Ravine, M.A., Caplinger, M.A., Ghaemi, F.T., Schaffner, J.a., Malin, M.C., Mahanti, P., Bartels, A., Anderson, J., Tran, T.N., Eliason, E.M., McEwen, A.S., Turtle, E., Jolliff, B.L., Hiesinger, H., 2010. Lunar reconnaissance orbiter camera (LROC) instrument overview. Space Sci. Rev. 150, 81–124. doi:10.1007/s11214-010-9634-2.

Runyon, K.D., Barnouin, O.S., 2016. Ejecta emplacement in the lab. Lunar and Planetary Science Conference XLVII Abstract #1075 doi:10.1038/ngeo2474.

Runyon, K.D., Barnouin, O.S., 2014. Experimental ejecta emplacement: early results. Lunar and Planetary Science Conference XLV Abstract #1071 doi:10.1029/2004JE002295.

Schmidt, R.M., Housen, K.R., 1987. Some recent advances in the scaling of impact and explosion cratering. Int. J. Impact Eng. 5, 543–560. doi:10.1016/0734-743X(87)90069-8.

Schultz, P.H., 1992. Atmospheric effects on ejecta emplacement and crater formation on Venus from Magellan. J. Geophys. Res. 97, 16183–16248.

Schultz, P.H., Anderson, R.R., 1996. Asymmetry of the Manson impact structure: evidence for impact angle and direction. Geol. Soc. Am. Spec. Pap. 302, 397–417. doi:10.1130/0-8137-2302-7.397.

Shoemaker, E.M., 1965. Preliminary Analysis of the Fine Structure of the Lunar Surface in Mare Cognitum Ranger VII (Technical Rep. No. 32-700).

Shuvalov, V., 2012. A mechanism for the production of crater rays. Meteorit. Planet. Sci. 47, 262–267. doi:10.1111/j.1945-5100.2011.01324.x.

Speyerer, E.J., Povilaitis, R.Z., Robinson, M.S., Thomas, P.C., Wagner, R.V., 2016. Quantifying crater production and regolith overturn on the Moon with temporal imaging. Nature 538, 215–218. doi:10.1038/nature19829.

Tornabene, L.L., Moersch, J.E., McSween, H.Y., McEwen, A.S., Piatek, J.L., Milam, K.A., Christensen, P.R., 2006. Identification of large (2–10km) rayed craters on Mars in THEMIS thermal infrared images: implications for possible Martian meteorite source regions. J. Geophys. Res. E Planets 111, 1–25. doi:10.1029/2005JE002600.

van der Bogert, C.H., Hiesinger, H., Dundas, C.M., Krüger, T., McEwen, A.S., Zanetti, M., Robinson, M.S., 2017. Origin of discrepancies between crater size-frequency distributions of coeval lunar geologic units via target property contrasts. Icarus 298, 49–63. doi:10.1016/j.icarus.2016.11.040.

Vickery, A.M., 1987. Variation in ejecta size with ejection velocity. Geophys. Res. Lett. 14, 726–729. doi:10.1029/GL014i007p00726.

Werner, S.C., Medvedev, S., 2010. The Lunar rayed-crater population–characteristics of the spatial distribution and ray retention. Earth Planet. Sci. Lett. 295, 147–158. doi:10.1016/j.epsl.2010.03.036.

Zeller, E.J., Ronca, L.B., 1967. Space weathering of lunar and asteroidal surfaces. Icarus 7, 372–379.